PAPER

Photocatalytic-induced bubble-propelled isotropic g-C₃N₄-coated carbon microsphere micromotors for dynamic removal of organic pollutants†

Xiaoyi Song,[a] Yulian Tao,[a] Jialiang Liu,[a] Jian Lin,[a] Pingqiang Dai,[a] Qianting Wang,[a] Wei Li,[ab] Wenzhe Chen[a] and Chan Zheng [ID] *[ab]

An isotropic bubble-propelled graphitic carbon nitride coated carbon microsphere (g-C₃N₄@CMS) micromotor that displays efficient self-propulsion powered by visible light irradiation and offers effective dynamic removal of organic pollutants for environmental applications is described. Its morphology, structure, and composition were systematically characterized, confirming the successful coating of g-C₃N₄ on the CMS surface and a core−shell structure. The photocatalytic-induced bubble propulsion of g-C₃N₄@CMS micromotors essentially stems from the asymmetrical photocatalytic redox reactions of g-C₃N₄ on the symmetrical surface of micromotors under visible light illumination. The stacking effect of g-C₃N₄ on the CMS surface results in a microporous structure that provides a highly reactive photocatalytic layer, which also leads to effective bubble evolution and propulsion at remarkable speeds of over 167.97 $\mu m\ s^{-1}$ under 250 mW cm^{-2} visible light in the presence of 30% H₂O₂ fuel. The velocity can be easily and effectively adjusted by H₂O₂ fuel and the intensity of visible light. Furthermore, the motion state can be reversibly and wirelessly controlled by "switching on/off" light. Such coupling of the high photocatalytic activity of the porous g-C₃N₄ shell with the rapid movement of these light-driven micromotors, along with the corresponding fluid dynamics and mixing, result in greatly accelerated organic pollutant degradation. The adsorption kinetics have also been investigated and shown to follow pseudo-second-order kinetics. The strategy proposed here would inspire the designing of light-driven symmetrical micromotors because of the low cost, single component, and simple structure as well as facile and large-scale fabrication, which make them suitable for practical applications.

1 Introduction

In recent decades, environmental problems, especially water pollution, have caused widespread and serious threats to public health and natural ecosystems due to rapid industrialization and population growth. Various pollutants, mainly from industrial production, are inevitably released into natural water bodies, especially refractory organic pollutants, which are harmful to ecological systems and seriously endanger human health. To solve these environmental problems, many techniques have been developed including various chemical, biological, and physical methods.[1–6] Among these methods, light-driven micromotors, which can harvest and convert light irradiation for inducing their mechanical propulsion, are especially appealing in photocatalytic pollutant degradation owing to the

combination of motion-induced mixing enhancement and their intrinsic catalytic character.[7–11] For example, Wu *et al.* described a kind of TiO₂–Au Janus micromotor which can effectively degrade methyl blue, cresol red and methyl orange.[12] Using Au–WO₃@C Janus micromotors, dye pollutants were removed under UV light as well.[13] Wang *et al.* reported that a light-powered TiO₂–Fe Janus micromotor with photocatalytic and Fenton reactions for efficient degradation of organic pollutants in polluted water.[14]

According to the propulsion mechanism, light-driven micromotors can be mainly categorized as self-electrophoresis, self-diffusiophoresis, bubble recoil, thermophoresis, and deformation propulsion.[15–17] Among them, photocatalyst-based micromotors are the primary strategy to construct light-driven micromotors, and the design, fabrication, and application of semiconducting photocatalysts such as TiO₂, ZnO, and WO₃ are most involved owing to their chemical stability and high photocatalytic activity.[18–21] However, the above-mentioned semiconductors only respond to UV irradiation, which is low in sunlight and harmful to human beings, because of the relatively large bandgap value. As a consequence, alternative visible-light-activated photocatalytic micromotors

[a]School of Materials Science and Engineering, Fujian University of Technology, 3 Xueyuan Road, Fuzhou 350108, PR China. E-mail: czheng.fjut@gmail.com

[b]Institute of Materials Surface Technology, Fujian University of Technology, 3 Xueyuan Road, Fuzhou 350108, PR China

† Electronic supplementary information (ESI) available. See https://doi.org/10.1039/d2ra01577c

have been developed because visible light is a ubiquitous, clean, and long-lasting fuel source. More importantly, the potential use of visible light radiation as the energy source to drive the movement of micromotors and for environmental remediation makes it the most attractive self-sustainable technology of the future. Therefore, several studies have been carried out to expand the light wavelength to the visible region of the spectrum and narrow bandgap semiconductor materials including Cu_2O and $BiOI$ have been used.[22,23]

Recently, two-dimensional polymeric graphitic carbon nitride (g-C_3N_4), a conjugated polymer semiconductor, has attracted worldwide attention in environmental photocatalysis because of its unique optoelectronic properties, high chemical stability, good visible light absorption, biocompatibility, low cost, facile synthesis, and moderate energy gap ($\sim$2.7 eV).[24–26] These unique and versatile properties make g-C_3N_4 a potential candidate in hydrogen generation, CO_2 activation, degradation of organic pollutants, and sensing applications.[27,28] Unfortunately, to our knowledge, there are only two examples that demonstrate the use of g-C_3N_4 material for building micromotors. Pumera and co-workers presented g-C_3N_4-based tubular micromotors able to decompose H_2O_2 into oxygen bubbles, and then move by a photocatalytic-induced bubble-propelled mechanism under visible light irradiation.[29] In addition, tubular g-C_3N_4 micromotors can remove heavy metal ions from contaminated water. Zhang and colleagues reported a unique light-powered Pt-g-C_3N_4-based micromotor with water as the fuel.[30] Furthermore, the micromotor's motion behavior, *i.e.*, the on-off motion, the directional motion, and the moving velocity can be regulated by the irradiating light. Despite this progress, it is still challenging to explore the light-driven micromotors that use g-C_3N_4 as phototactic materials in polluted water treatment, which would promote a better understanding of the g-C_3N_4 propulsion mechanism and future optimization of the design of the light-activated g-C_3N_4 micromotors for potential environmental applications.

Herein, we propose an isotropic light-driven micromotor that is propelled based on a bubble-recoil motion mechanism. The micromotor is rationally assembled of a two-dimensional porous g-C_3N_4 shell on a carbon microsphere template to form a g-C_3N_4@carbon microsphere (g-C_3N_4@CMS) core–shell nanostructure by a simple and facile chemical solution route, exhibiting precise self-propulsion under visible light illumination. The synthetic procedure is facile, cost-effective, and metal-free, which could be applied to large-scale production. Such an isotropic core–shell architecture of a g-C_3N_4@CMS micromotor provides self-propulsion characteristics, high and stable visible-light-responsive photocatalytic effect, and then accelerates the degradation of organic pollutants efficiently. The light-induced bubble propulsion and degradation mechanism were also explored in detail.

2 Experimental

2.1. Materials

Melamine, glucose, ethanol, cetyltrimethylammonium bromide (CTAB, 99%), hydrogen peroxide (H_2O_2, 30%), sodium dodecyl sulfate (SDS), ethanol, and rhodamine B (RhB) were purchased commercially and used without any purification. Deionized water was obtained using a Milli-Q Direct 8.

2.2. Preparation of g-C_3N_4@CMS micromotors

2.2.1. Preparation of g-C_3N_4. Melamine was placed in a crucible and heated to 550 °C in a muffle furnace at a heating rate of 10 °C min^{-1}. This temperature was maintained for 2 h and the furnace was then cooled to room temperature. After firing, the samples were ground into powder to obtain the g-C_3N_4 powder.

2.2.2. Preparation of CMSs. Specifically, 6.3 g glucose and 1 g CTAB were added to 45 mL of deionized water under magnetic stirring for 15 min and ultrasonic irradiation for 5 min. The above mixture were transferred to a 50 mL Teflon reactor and hydrothermal at 180 °C for 8 h. After hydrothermal, the sample was centrifuged at 5000 rpm for 3 min, then washed with deionized water and anhydrous ethanol five times. Then, the black CMS powder was obtained by vacuum drying at 80 °C for 1 h.

2.2.3. Preparation of g-C_3N_4@CMS micromotors. Specifically, 100 mg g-C_3N_4 powder and 500 mg CMSs were added to a reaction kettle containing 80 mL deionized water, and the water was heated at 210 °C for 6 h. The samples were filtered and dried, heated to 200 °C for 4 h at a rate of 5 °C min^{-1} in a N_2 atmosphere, and cooled to room temperature with the furnace.

2.3. Characterizations

The morphologies and elemental distributions of the g-C_3N_4@CMS micromotors were investigated using field-emission scanning electron microscopy (FE-SEM; JEOL JSM-6700, JEOL Ltd., Tokyo, Japan) combined with energy-dispersive X-ray spectroscopy (EDX; Oxford X-MAN spectrometer). The sample surfaces were sputtered with Au before the SEM observations. Crystallographic information was obtained by performing X-ray diffraction (XRD; Bruker D8-Advance) with a Cu Kα radiation source ($\lambda = 1.5418$ Å) at 40 kV and 30 mA, over the 2θ range 10° to 90°. An STA449F3 synchronous thermal analyzer (Netstal, Germany) was used to investigate the thermal stability of the micromotors. In these experiments, each sample was examined over the temperature range 20–800 °C at a heating rate of 10 °C min^{-1} in air. The pore structures of the assembled architectures were determined from N_2 adsorption isotherms at 77 K using a surface area and porosimetry analyzer (Micromeritics 3Flex Surface area and Porosity Analyzer, USA). The samples were degassed at 80 °C for 12 h before recording the isotherms. X-ray photoelectron spectroscopy (XPS, Escalab 250, Thermo Fisher Scientific Co., USA) used Al Kα radiation, and the binding energy of each element was calibrated to the 284.8 eV C 1s peak.

2.4. Characterization of micromotor motion

During each driving experiment, a Nikon ECLIPSE E100 microscope with a 10 eyepiece and 4 and 10 objective lens was used to examine the motors under exposure to blue light (420 nm, 250 mW cm^{-2}) and immersion in an aqueous solution

containing 5, 10, 15, 20, 25, and 30 wt% H_2O_2 and 1 wt% SDS. A digital camera (PSC601-10C, OPLENIC) was used to examine the sample microstructures, and the motor movement was assessed using a video capture program (OPLENIC).

2.5. Degradation of rhodamine B

The degradation experiment of RhB was carried out using a g-C_3N_4@CMS micromotor. Add 20 mg sample to 50 mL mixed solution containing RhB (10 mg L^{-1}), H_2O_2 (3 wt%), and SDS (0.125 wt%), and irradiate the mixed solution with a xenon lamp (Newport AM 1.5) as the light source (equipped with a 420–780 nm filter). The degradation of RhB under these conditions was observed. The absorbance of RhB was measured every 10 min with a UV-2600 spectrophotometer. The concentration of RhB was calculated according to the standard absorbance curve of RhB. The degradation curve of RhB with time was obtained according to the ratio of residual RhB concentration to original RhB concentration.

The cyclic adsorption performance test of RhB was carried out using a g-C_3N_4@CMS micromotor. The g-C_3N_4@CMS micromotor with adsorbed pollutant solution was cleaned 4 times alternately with deionized water and anhydrous ethanol, and the cleaning process was separated by centrifuge at 8000 RPM. The separated products were dried in an oven at 60 °C. After drying, the degradation adsorption experiment was carried out again under the original conditions. The whole degradation process was repeated five times.

3 Results and discussion

3.1. Preparation of g-C_3N_4@CMS micromotors

In general, an asymmetric shape or composition is necessary for micromotors to initiate their propulsion as a result of a photocatalytic product's gradient buildup, and a Janus type or tubular shape is usually involved. The existing methods to obtain Janus and tubular structures comprise either troublesome multistep processes or sometimes require the utilization of expensive equipment to engineer various asymmetric products. To explore a facile and efficient strategy for the continuous fabrication of light-driven micromotors, we developed symmetrical and spherical core–shell micromotors, which induced bubble propulsion by the optical orientation of light.

The procedure for the fabrication of the g-C_3N_4@CMS micromotors is illustrated in Scheme 1. Briefly, metal-free graphite-like g-C_3N_4 was fabricated from pyrolysis of melamine.
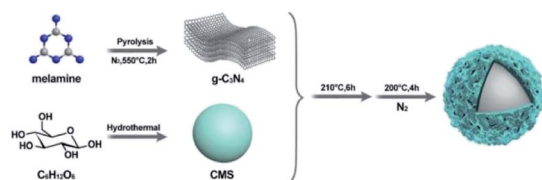
Scheme 1 Schematic diagram of the synthesis of photocatalytic g-C_3N_4@CMS micromotors.

(Fig. 1a), as a nitrogen-rich precursor. Subsequently, CMSs were synthesized through hydrothermal methods using glucose as the precursor. Uniform CMSs with a diameter of about 10 μm and homogeneous distribution display smooth surfaces (Fig. 1b and c). Subsequent hydrothermal and annealing treatment of the obtained g-C_3N_4 and CMSs led to the formation of g-C_3N_4@CMS micromotors in large scale with uniformity, as can be confirmed by the SEM image in Fig. 1d and e. The CMS has been completely trapped by g-C_3N_4. The diameter of the g-C_3N_4@CMS micromotor is about 13 μm. Fig. 1f reveals the details of the surface characteristics of coating the g-C_3N_4 shell. The two-dimensional g-C_3N_4 are tightly packed together around the CMS. In addition, large numbers of micropores can be detected, which can be attributed to the stacked spaces of two-dimensional g-C_3N_4 and the evaporation of solvent during the heat treatment in a N_2 atmosphere. The EDX mapping images reveal the coexistent and uniform distribution of C and N elements in the g-C_3N_4@CMS micromotor (Fig. 1i and j), confirming the successful construction of the g-C_3N_4@CMS micromotors.

The chemical status and chemical composition of the CMS core, g-C_3N_4 shell, and g-C_3N_4@CMS micromotors were investigated using XPS to study the formation procedure of the micromotors. As is displayed in Fig. 2a, the survey spectrum reveals the presence of C, N, and O elements in the g-C_3N_4@CMS micromotors, demonstrating the introduction of g-C_3N_4. It is noted that the content of O element in CMSs drastically decreased after loading with g-C_3N_4. The C 1s high-resolution spectrum of CMSs can be deconvoluted into four peaks, centered at 284.4, 285.0, 286.0, and 287.4 eV (Fig. 2b), corresponding to sp^2 C=C bonds of graphitic carbon, C–O–H, C–O bond, and C=O bond, respectively, implying that the surface of CMSs is rich in carboxy and hydroxyl groups.[31,32] The N 1s high-resolution spectrum of g-C_3N_4 can be fitted to four peaks (Fig. 2e), which can be ascribed to C–N–C (398.6 eV), tertiary nitrogen N–(C)$_3$ (400.1 eV), N–H groups (401.2 eV), and π-excitations (404.3 eV).[33,34] Notably, the broad band at 401.2 eV mainly resulted from the terminal amino groups (C–N–H) owing to incomplete condensation in the process of thermal polymerization, which would react with the carboxy and hydroxyl groups on the CMS surface through a hydroxylation reaction and result in lamellar g-C_3N_4 self-assembly on CMSs,[35] and therefore the reduction of O content in g-C_3N_4@CMS micromotors. The above assumption can also be verified by the C 1s high-resolution spectrum in g-C_3N_4@CMS micromotors. As shown in Fig. 2d, the C 1s binding energy of g-C_3N_4@CMS micromotors mainly shows three peaks with binding energies of 288.4, 286.4, and 284.8 eV, which can be assigned to C–N–C groups of g-C_3N_4, g-C_3N_4 with absorbed H_2O (also can be found in C 1s of g-C_3N_4 in Fig. 2c), and C–C bonds of graphene, respectively.[36] A broad band at 285.0 eV (C–OH) present in CMSs cannot be detected. In addition, the N 1s spectrum distribution of g-C_3N_4@CMS micromotors is similar to that of g-C_3N_4 except for a slight shift of the peaks, as displayed in Fig. 2f, demonstrating the successful coating of g-C_3N_4 and an electrochemical interaction occurs between CMSs and g-C_3N_4 in the g-C_3N_4@CMS micromotors.

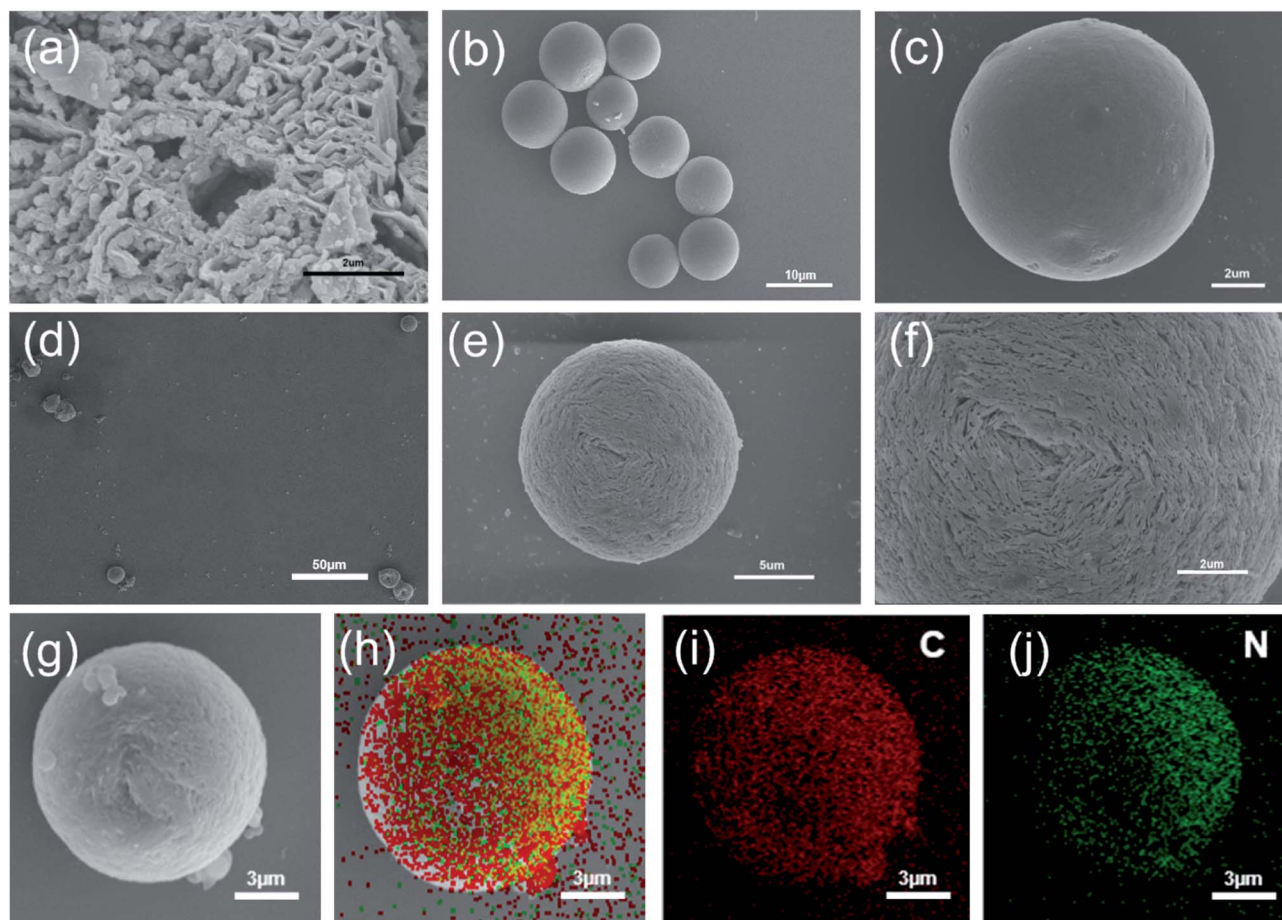**Fig. 1** Micromotor characterization. (a) SEM images of g-C_3N_4, (b) and (c) SEM images of CMS, (d), (e) and (f) SEM images of g-C_3N_4@CMS micromotor, (g–j) g-C_3N_4@CMS elemental distributions.

3.2. Characterization of g-C_3N_4@CMS micromotors

The crystal structures of g-C_3N_4@CMS micromotors and pristine g-C_3N_4 were characterized by the XRD pattern (Fig. 3a). The XRD pattern confirmed the formation of graphitic stacking C_3N_4. The sharp diffraction peak at 27.4° and broad diffraction peak at 13.1° in the pristine g-C_3N_4 respectively corresponded to the (002) reflection of the stacking of the conjugated aromatic system and (100) reflection of in-plane structural packing motif of tri-s-triazine units.[37] The g-C_3N_4@CMS micromotors show a similar XRD pattern as pristine g-C_3N_4, indicating the existence of g-C_3N_4 in the micromotors.

The chemical structure of the g-C_3N_4@CMS micromotors and g-C_3N_4 were investigated using FT-IR spectroscopy. As displayed in Fig. 3b, the absorption peak at 808 cm^{-1} in both samples is ascribed to typical tri-s-triazine units (C-N-HC and C=N stretching). The absorption bands between 1150 and 1480 cm^{-1} are attributed to the typical vibrations of C–N heterocycles associated with skeletal stretching vibrations of aromatic rings.[38] The peaks observed at 1570–1640 cm^{-1} are mainly due to the presence of C=N bonds.[39] The broad bands centered at 3000–3500 cm^{-1} correspond to uncondensed amine groups and surface-adsorbed water.[40] The characteristic peaks of g-C_3N_4@CMS micromotors are identical to the pristine g-

C_3N_4, implying the tri-s-triazine units are not destroyed during the hydrothermal process.

The nitrogen adsorption–desorption isotherms of CMSs and g-C_3N_4@CMS micromotors are displayed in Fig. 3c. It can be seen that the N$_2$ adsorption–desorption curve of g-C_3N_4@CMS micromotors has an obvious adsorption hysteresis loop and the hysteresis ring has no saturated adsorption platform and belongs to type H3 hysteresis ring, which is a typical characteristic of mesoporous materials.[41] The pore size distribution of the samples evaluated using the Barrett–Joyner–Halenda adsorption method in Fig. 3d further confirms the formation of mesopores. Apparently, g-C_3N_4@CMS micromotors exhibit trimodal mesopores due to the pores in the two-dimensional g-C_3N_4 nanoflakes and the space between the nanoflakes. The quantitative analysis of the specific surface area of g-C_3N_4@CMS micromotors calculated it to be 9.64 m^2 g^{-1}, which is a significant increase over CMSs (1.73 m^2 g^{-1}) after the introduction of g-C_3N_4 because of the pores in g-C_3N_4 and stacking effect. The resultant hybrid structure might provide novel optoelectronic properties. The optical characteristics of g-C_3N_4@CMS micromotors and g-C_3N_4 were investigated using.

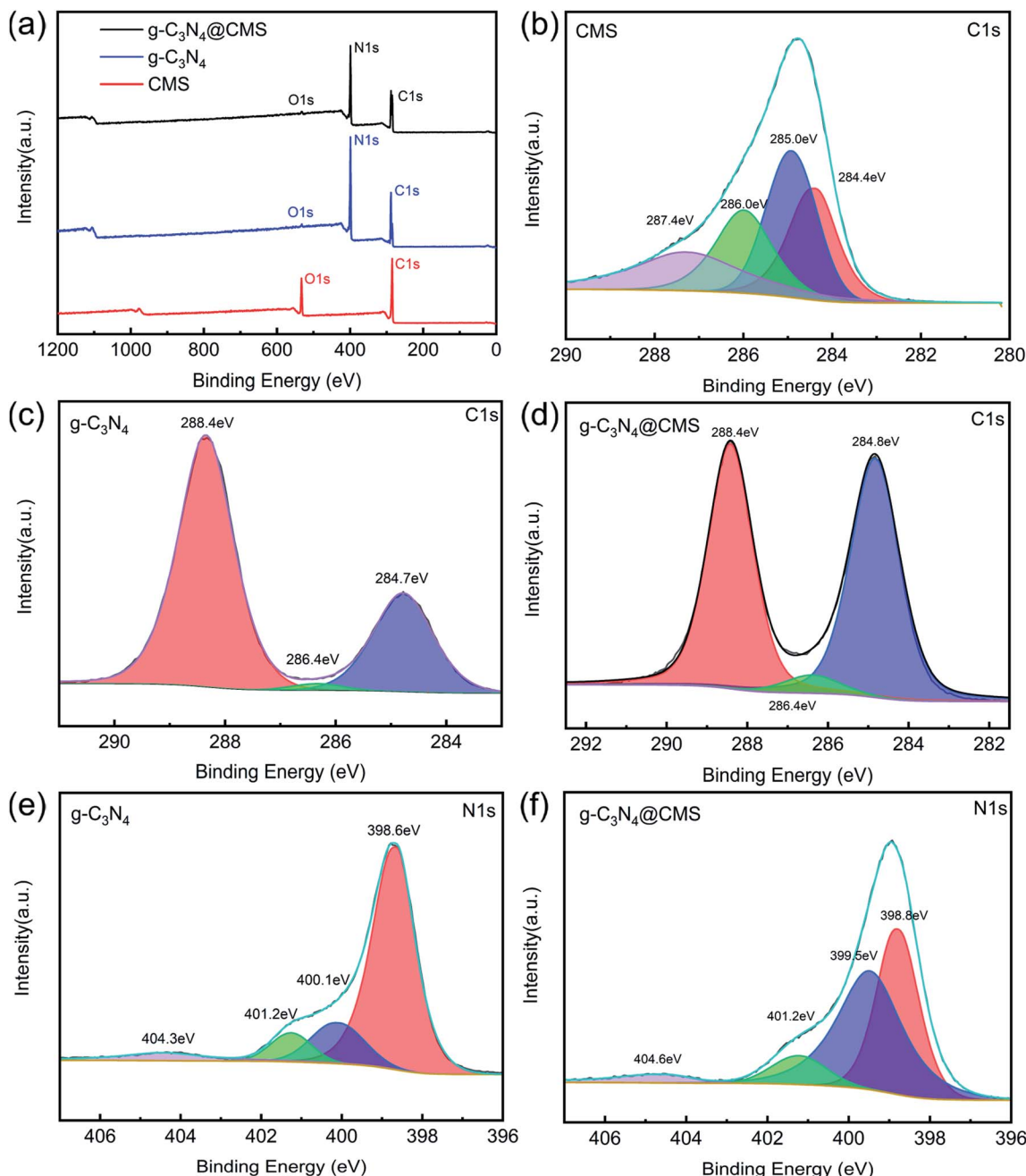UV-vis diffuse reflectance spectra. As presented in Fig. 4a, both samples feature an intrinsic semiconductor-like

Fig. 2 (a) XPS survey spectrum of CMS, g-C$_3$N$_4$ and g-C$_3$N$_4$@CMS, (b−d) C 1s high-resolution spectrum of CMS, g-C$_3$N$_4$ and g-C$_3$N$_4$@CMS, (e, f) N1s high-resolution spectrum of g-C$_3$N$_4$ and g-C$_3$N$_4$@CMS.

absorption in the blue region of the visible spectra. With the introduction of g-C$_3$N$_4$, the g-C$_3$N$_4$@CMS micromotors display an evident blueshift of the absorption edge. The band gap of the g-C$_3$N$_4$ and the g-C$_3$N$_4$@CMS micromotors can be determined from the following equation:

$$\alpha h\nu = A(h\nu - E_g)^n \tag{1}$$

where α, h, ν, and E_g represent the absorption coefficient, Planck's constant, frequency of light, and the band gap, A and n are constants, respectively. The bandgap energy (E_g) estimated

from the intercept of the tangents to the plots of $(\alpha h\nu)^{1/2}$ vs. photon energy are 2.44 and 2.72 eV for g-C$_3$N$_4$@CMS micromotors and g-C$_3$N$_4$, respectively, as shown in Fig. 4b. The bandgap calculated herein for g-C$_3$N$_4$ is consistent with the literature values.[42] The blueshift of the absorption band and narrow bandgap might be attributed to interface interaction between g-C$_3$N$_4$ and CMSs, and the formation of C=N–C and –CN chemical bonds. The narrow bandgap would be able to make the most of visible light and produce photogenerated charge carriers more effectively, resulting in higher photocatalytic activity.[43]
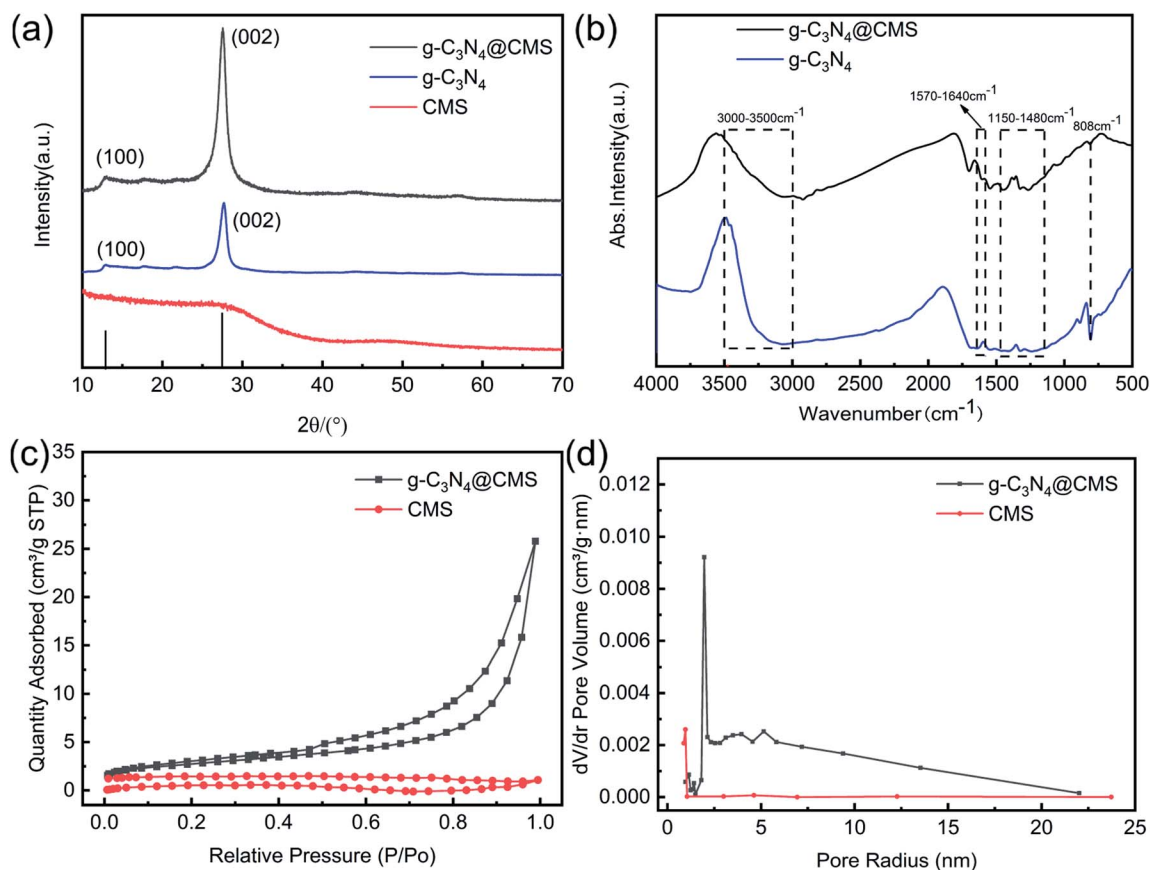
Fig. 3 (a) XRD patterns of g-C$_3$N$_4$ and g-C$_3$N$_4$@CMS; (b) Fourier transform infrared spectra of g-C$_3$N$_4$ and g-C$_3$N$_4$@CMS; (c) N$_2$ adsorption–desorption isotherms for CMS and g-C$_3$N$_4$@CMS; (d) pore size distribution of theCMS and g-C$_3$N$_4$@CMS.
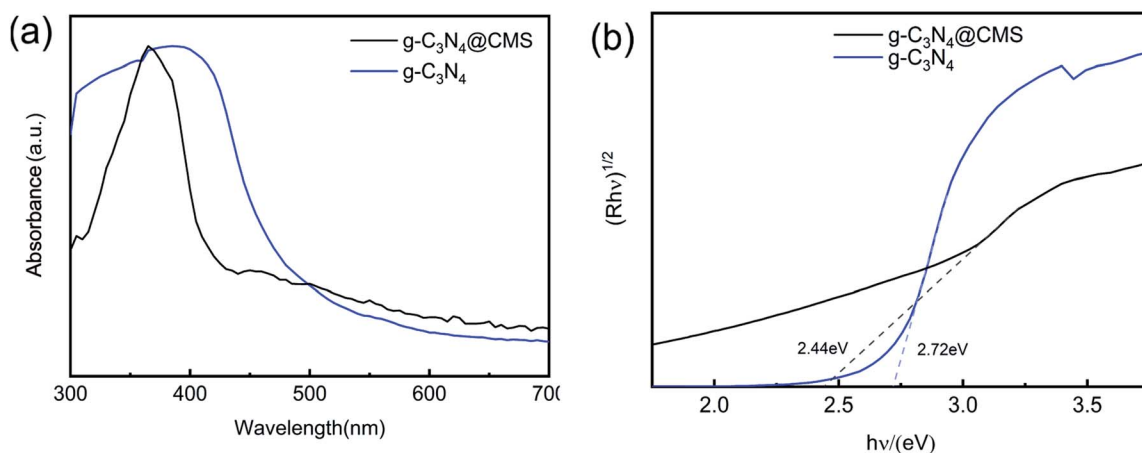

Fig. 4 (a) UV-Vis diffuse absorbance spectra of the g-C$_3$N$_4$ and g-C$_3$N$_4$@CMS. (b) Plotting of (a) in the $(\alpha h\nu)^{1/2} \sim$ energy coordinate to evaluate the corresponding bandgap of the g-C$_3$N$_4$ and the g-C$_3$N$_4$@CMS.

3.3. Self-propulsion of g-C$_3$N$_4$@CMS micromotors

We next evaluated the photoactivated self-propulsion of g-C$_3$N$_4$@CMS micromotors in bubble mode. The time-lapse images of Fig. 5a–d and ESI Video 1† illustrate the propulsion of the micromotor in 30% H$_2$O$_2$ solution and the power density of visible light is 250 mW cm^{-2} with a wavelength of $\lambda =$ 420 nm. To improve the observation of the motor motion, 1% SDS was added as a surfactant to decrease the interfacial free energy and thus facilitate bubble formation and detachment from the surfaces of the micromotors. A long tail of bubbles is released from one side of the micromotor, confirming the bubble-induced self-propulsion under visible light irradiation.
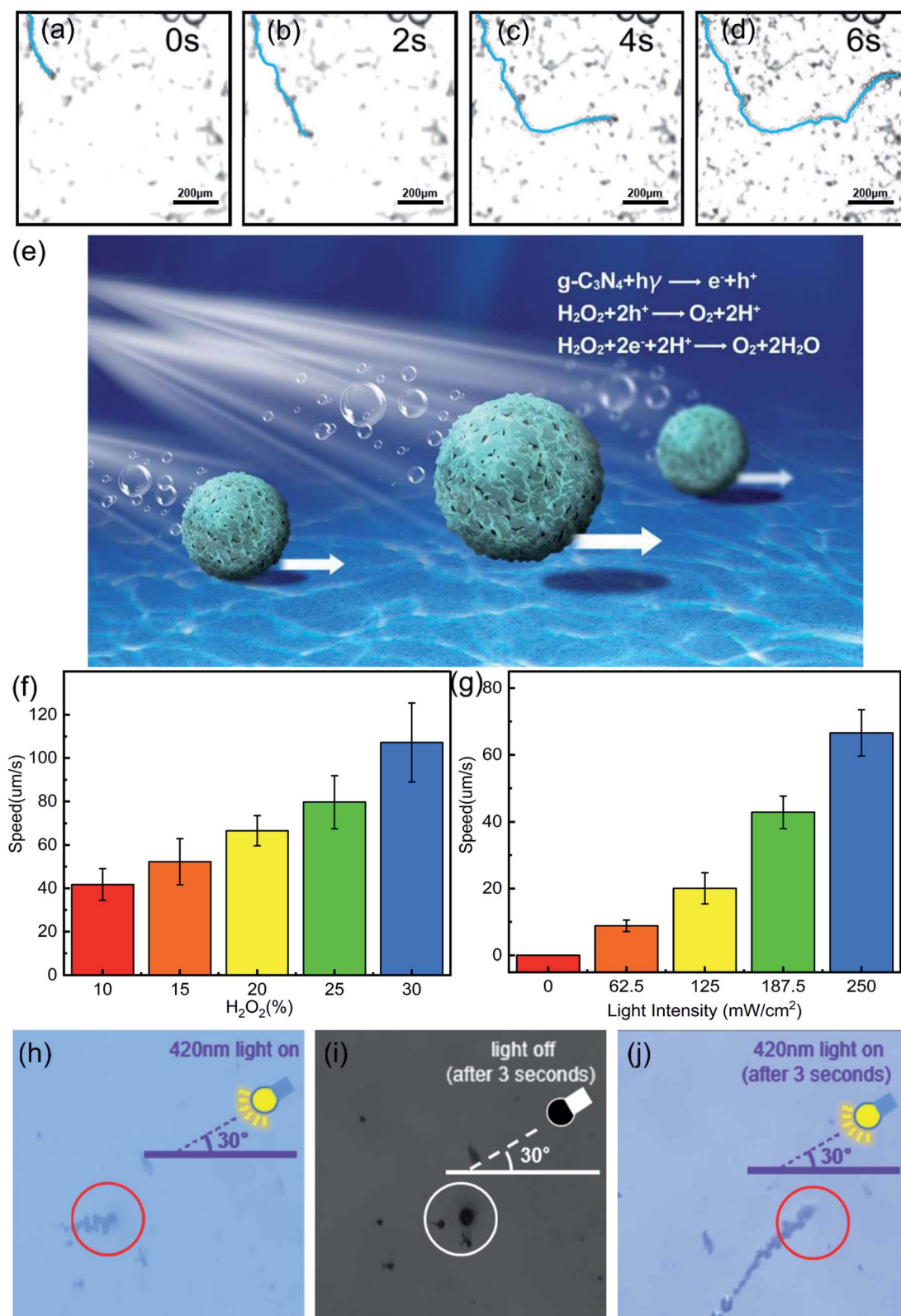
Fig. 5 (a–d) g-C$_3$N$_4$@CMS motion video screenshots at different times (0s,2s,4s,6s) under 420 nm light; (e) schematic representation of the self-propulsion by g-C$_3$N$_4$@CMS micromotors; (f) speed of g-C$_3$N$_4$@CMS micromotor *versus* H$_2$O$_2$ concentration; (g) speed of g-C$_3$N$_4$@CMS micromotor *versus* light intensity; (h–j) the influence of light on the motion of g-C$_3$N$_4$@CMS micromotor.

Paper

In addition, the maximum velocity of the light-driven micromotor can be estimated to be around 167.97 μm s^{-1}. As reported previously, similar isotropic TiO$_2$ microparticles can be propelled through nonelectrolyte self-diffusiophoresis in an aqueous solution.[4] In the present work, the bubble self-propulsion is mainly due to asymmetrical photocatalytic redox reactions of g-C$_3$N$_4$ on the symmetrical surface of micromotors under visible light illumination, as schematically shown in Fig. 5e. When visible light irradiated the spherical g-C$_3$N$_4$@CMS micromotor, because of the limited penetration depth of the irradiating light, it would generate a light side and a shadow side. On the light side, considering that the Eg of the g-C$_3$N$_4$@CMS micromotors (2.44 eV) is lower than that of the irradiation energy (2.95 eV), the electrons present in the valence band (VB) of g-C$_3$N$_4$ would transfer to the corresponding conduction band, generating a hole in the VB, given by eqn (2). Subsequently, these photogenerated holes and electrons could react with H$_2$O$_2$ to produce O$_2$, as given by eqn (3) and (4). Then, an asymmetrical surface on the isotropic g-C$_3$N$_4$@CMS micromotors is formed and oxygen is released from the light side of the g-C$_3$N$_4$@CMS micromotor, which subsequently results in the active motion of the micromotors *via* bubble recoil. Furthermore, the stacking effect of g-C$_3$N$_4$ on the CMS surface results in a microporous structure to provide a highly reactive photocatalytic layer, which also leads to effective bubble evolution and propulsion at a remarkable speed.

$$\text{g-C}_3\text{N}_4 + h\nu \rightarrow \text{e}^- + \text{h}^- \tag{2}$$

$$\text{H}_2\text{O}_2 + 2\text{h}^+ \rightarrow \text{O}_2 + 2\text{H}^+ \tag{3}$$

$$\text{H}_2\text{O}_2 + 2\text{e}^- + 2\text{H}^+ \rightarrow \text{O}_2 + 2\text{H}_2\text{O} \tag{4}$$
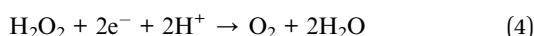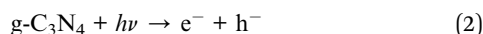
As discussed above, the self-propulsion of g-C$_3$N$_4$@CMS micromotors is mainly dependent on the O$_2$ produced by the decomposition of H$_2$O$_2$ fuel by photogenerated electron–hole pairs. Therefore, the speed of the g-C$_3$N$_4$@CMS micromotors is strongly dependent on the peroxide fuel concentration (ESI Videos 1–5† and Fig. 5f). The speed increased from 41.71 μm s^{-1} to 107.22 μm s^{-1} when the H$_2$O$_2$ fuel concentration increased from 10% to 30%. According to eqn (2) and (3), more H$_2$O$_2$ would induce release of more O$_2$ bubbles from the surface of micromotors, which act as the driving force of the micromotors and therefore increase their velocity. Meanwhile, the relationship of the irradiated visible light intensity (*I*) between the motion speed of the micromotors was also explored (ESI Videos 3, 6–9,† and Fig. 5g). ESI Videos 6† show that there are no bubbles and motion observed for g-C$_3$N$_4$@CMS micromotors when there is no visible light. When I increases from 62.5 to 250 mW cm^{-2}, the speed of the micromotor increases from 8.82 to 66.59 μm s^{-1}. Reported work revealed that adjusting light intensity will change the photon flux on the micromotors,[44] and thus increase the number of photogenerated holes and electrons in g-C$_3$N$_4$. Consequently, the photogenerated holes and electrons could de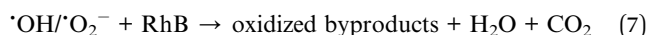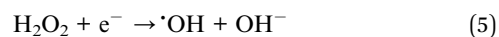compose more H$_2$O$_2$ fuel and then produce more O$_2$ bubbles and the speed of the micromotors is accordingly increased.

Another important characteristic of light-driven micromotors is the light-controlled on/off response. Usually, micromotors exhibit only slow random motion in the absence of light, but immediately start to move when the light is switched on. As can be seen from Fig. 5h–j and Video S10,† the bubble generation and motion of g-C$_3$N$_4$@CMS micromotors can be stopped by switching the light off and immediately reactivated by switching the light on again. This repeatable and controllable motion of micromotors can be achieved by switching the visible radiation on or off and can be useful in a range of applications.

3.4. Degradation of RhB by g-C$_3$N$_4$@CMS micromotors

Recently, g-C$_3$N$_4$ has shown good photocatalytic performance for the decomposition of some hazardous organic compounds and has been extensively applied in environmental areas.[45,46] Meanwhile, micromotors have been shown to be potentially promising candidates for pollutant removal owing to the autonomous movement of a micromotor promoting contact between the photocatalyst/adsorbent and target pollutant or better release and dispersion of the functioning agents for the chemical remediation process, and therefore the degradation efficiency improves significantly.[47,48] To prove the potential application of g-C$_3$N$_4$@CMS micromotors in environmental pollution fields, the pollutant removal performance of g-C$_3$N$_4$@CMS micromotors was evaluated. RhB, a typical organic dye, was chosen as the target pollutant. Before the experiment, the micromotors were placed in the dark for 30 min to eliminate the influence of RhB adsorption by g-C$_3$N$_4$@CMS on the photocatalytic degradation.

The degradation of the RhB solution in the presence of the micromotors is apparent, as confirmed by the disappearance of the red solution color after degrading for 60 min, as shown in Fig. 6a. Meanwhile, the UV-vis spectroscopy of RhB after different reaction times is also shown in Fig. 6c. The characteristic absorption peak of RhB molecules at 553 nm gradually decreased as time increased, and the removal of RhB reached 95.88% after 60 min, indicating that the g-C$_3$N$_4$@CMS micromotors possess excellent degradation ability. Fig. 6b schematically illustrates the process of photocatalysis of g-C$_3$N$_4$@CMS micromotors under visible light irradiation. In addition to the species formed in the reactions shown in eqn (2) and (4), reactive oxygen species such as hydroxyl radicals (˙OH) and superoxide radicals (˙O$_2^-$) can be formed during the self-propulsion in the presence of H$_2$O$_2$ fuel, as shown in eqn (5) and (6). The ˙OH and ˙O$_2^-$ are mainly responsible for the oxidative degradation of RhB and generation of CO$_2$, H$_2$O, and other nontoxic oxidized byproducts.

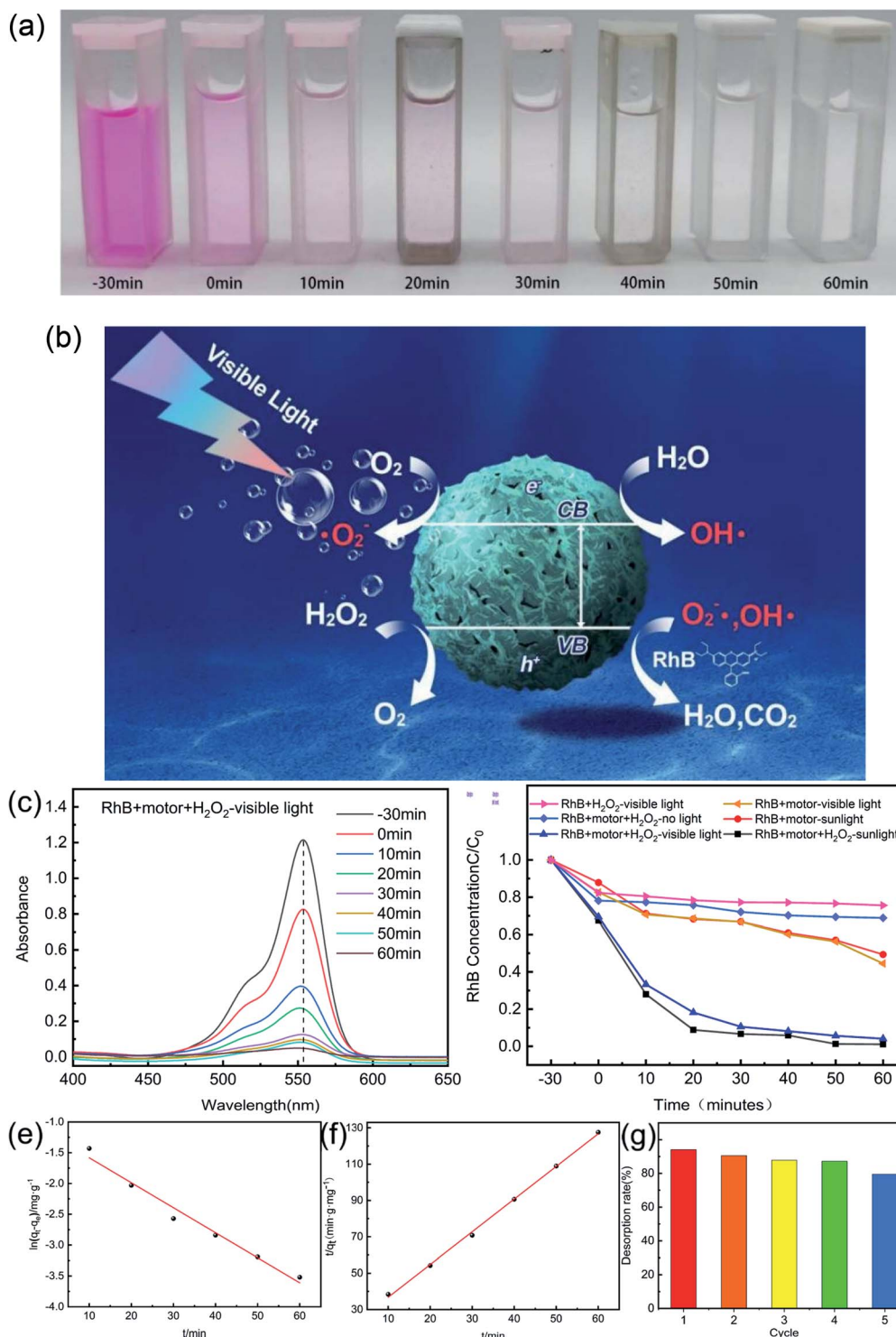$$\text{H}_2\text{O}_2 + \text{e}^- \rightarrow \text{˙OH} + \text{OH}^- \tag{5}$$

$$\text{O}_2 + \text{e}^- \rightarrow \text{˙O}_2^- \tag{6}$$

$$\text{˙OH/˙O}_2^- + \text{RhB} \rightarrow \text{oxidized byproducts} + \text{H}_2\text{O} + \text{CO}_2 \tag{7}$$

Fig. 6 (a) Photographs of the oxidation of RhB after 60 min treatment with g-C$_3$N$_4$@CMS micromotor; (b) schematic representation of the self-propulsion and the catalytic degradation of RhB by g-C$_3$N$_4$@CMS micromotor; (c) the absorbance spectra of RhB after 60 min treatment with g-C$_3$N$_4$@CMS micromotor; (d) the degradation of RhB under different conditions; (e) quasi-first-order and (f) quasi-second-order kinetics models for RhB degradation in g-C$_3$N$_4$@CMS micromotor. (g) Test results of cyclic degradation of rhodamine B by micromotors.

A series of control experiments was next performed in parallel to demonstrate the advantage of g-C$_3$N$_4$@CMS micromotors, and the results are shown in Fig. 6d. It is worth mentioning that the initial concentration of RhB was the same in all the degradation experiments. In the absence of the g-C$_3$N$_4$@CMS motors, remediation extent with only H$_2$O$_2$ irradiated with visible light was 24.38%, which can be attributed to the fact that the photodegradation of H$_2$O$_2$ could also produce

free radicals and degrade RhB to some extent. The g-C$_3$N$_4$@CMS micromotors with only H$_2$O$_2$ in the absence of visible light illumination cannot induce the photocatalytic reactions of g-C$_3$N$_4$ and only show removal efficiency of 31.10% as expected. Moreover, the micromotors with visible light irradiation in the absence of H$_2$O$_2$ show removal efficiency of 55.48%, the degradation of RhB is essentially due to the photocatalytic effect of g-C$_3$N$_4$. However, the motors could not move, and the lack of active motion greatly limited the degradation capability. Especially, when all conditions were included, *i.e.*, g-C$_3$N$_4$@CMS micromotors, H$_2$O$_2$, and visible light, the system shows the highest removal efficiency of 95.88% in 60 min, which was two times that of unpropelled counterparts. This is mainly attributed to the fact that H$_2$O$_2$ could provide the fuel to induce active motion and thus could speed up the solution mixing process, and meanwhile, the decomposition of H$_2$O$_2$ could also produce free radicals. Both procedures would accelerate the dye-degradation process. The effect of H$_2$O$_2$ was further confirmed by the comparison experiments by irradiation with simulated sunlight. The degradation efficiency of micromotors with H$_2$O$_2$ can reach 98.91% in 60 min whereas it only degraded 50.64% of RhB in the absence of H$_2$O$_2$. Therefore, our results demonstrated that although the g-C$_3$N$_4$ shell could generate hydroxyl radicals because of photocatalytic activity, the self-propulsion of the motors is crucial for providing micromixing to make many more active sites contact the model pollutant, thereby resulting in a much faster dye-degradation rate. In addition, the porous structural characteristic of g-C$_3$N$_4$@CMS micromotors would also contribute to the degradation efficiency. As can be seen from Fig. 1f, large numbers of micropores exist on the surface of the rough g-C$_3$N$_4$ shell. Under visible/sunlight irradiation, the micropores would adsorb the dye molecules, serve as the oxidizing agents, and then degrade the dye molecules. Therefore, the micropores present on the surface of the g-C$_3$N$_4$@CMS micromotors could also facilitate the degradation procedure.

To gain further insight into the adsorption mechanism, the photocatalytic degradation processes were then studied employing pseudo-first-order and pseudo-second-order kinetics models. The pseudo-first-order kinetics were calculated according to the following equation:

$$\ln(q_e - q_t) = \ln q_e - k_1 t \qquad (8)$$

where t is the adsorption time (min), q_e and q_t represent the adsorption capacity (mg g^{-1}) of the g-C$_3$N$_4$@CMS micromotor at RhB equilibrium and the adsorption capacity at time t, respectively; k_1 was used as the adsorption rate constant (min^{-1}) of the quasi-first-order kinetic model. Using $\ln(q_e - q_t)$ to plot the line, the slope and intercept of the line can be used to calculate the q_e value of the parameter and k_1. From Fig. 6a we can calculate the degradation rate constant $K_1 = 0.0406$ min^{-1}. The pseudo-second-order kinetics were expressed as follows:

$$\frac{t}{q_t} - \frac{1}{k_2 q_e^2} = \frac{t}{q_e} \qquad (9)$$

where k_2 is the adsorption rate constant (g (mg^{-1} min^{-1})) of the quasi-second-order kinetics model. The other parameters are the same as above. The slope and intercept of the line can be used to calculate the values of the parameters q_e and k_2. Fig. 6e and f present the linear fittings of the data obtained using the g-C$_3$N$_4$@CMS micromotors according to the above two models. The coefficient of determination (R^2) for the pseudo-second-order model (0.99867) was higher than that for the pseudo-first-order model (0.97755), suggesting that the g-C$_3$N$_4$@CMS micromotor tended to adsorb RhB through chemical processes, and that adsorption was dependent on both the surface properties of the adsorbent and the solute concentration.

In addition, we have performed the reusability of the micromotors. Degradation capability decreases as the number of recycling does, as shown in Fig. 6g. The degradation efficiency maintains at 79.5% even after five cycles, confirming that g-C$_3$N$_4$@CMS micromotors present good reuse ability.

4 Conclusions

In conclusion, we have presented an isotropic bubble-propelled g-C$_3$N$_4$@CMS micromotor powered by visible light irradiation for enhanced removal of organic pollutants for environmental applications. The morphology, structure, and composition were systematically characterized, confirming the successful coating of g-C$_3$N$_4$ on the CMS surface and the core–shell structure. The fabrication procedure would inspire novel micromotors because of the low cost, single component, and simple structure as well as the facile, large-scale fabrication. The isotropic g-C$_3$N$_4$@CMS micromotors can realize self-propulsion at a speed of 167.97 μm s^{-1} under 250 mW cm^{-2} visible light in the presence of 30% H$_2$O$_2$ fuel because of bubble recoil. The velocity can be easily and effectively adjusted by H$_2$O$_2$ fuel and the intensity of visible light. Furthermore, the motion state can be reversibly and wirelessly controlled by "switching on/off" light. Such coupling of the high photocatalytic activity of the porous g-C$_3$N$_4$ shell with the rapid movement of these light-driven micromotors, along with the corresponding fluid dynamics and mixing, results in greatly accelerated degradation of organic pollutants. The g-C$_3$N$_4$@CMS micromotors can degrade 95.88% of RhB in only 60 min under simulated visible light illumination, which is two times that of unpropelled counterparts. The adsorption mechanism has been shown to follow pseudo-second-order kinetics, thereby indicating that chemisorption of RhB occurs at the surface of the g-C$_3$N$_4$-coated micromotors. These isotropic and metal-free g-C$_3$N$_4$@CMS micromotors combining self-propulsion by light-induced bubble-propulsion mechanism and outstanding capabilities for organic dye pollution removal reported here are of importance for the design of new, fast, and low-cost photocatalytic-based micromotors for dynamic environmental remediation of organic compounds in wastewaters and industrial effluents.

Author contributions

Chan Zheng conceived the idea, initiated and supervised the project, discussed the results, and edited the manuscript. Xiaoyi

Notes and references

1 G. Tang, L. Chen, L. Lian, F. Li and C. Huang, *Chem. Eng. J.*, 2021, **407**, 127187.

2 J. Tong, D. Wang, D. Wang, F. Xu, R. Duan, D. Zhang, J. Fan and B. Dong, *Langmuir*, 2019, **36**, 6930–6937.

3 B. Jurado-Sanchez, J. Wang and A. Escarpa, *ACS Appl. Mater. Interfaces*, 2016, **8**, 19618–19625.

4 H. Jiang, X. He, Y. Ma, B. Fu, X. Xu, B. Subramanian and C. Hu, *ACS Appl. Mater. Interfaces*, 2021, **13**, 5406–5417.

5 R. Maria-Hormigos, M. Pacheco, B. Jurado-Sánchez and A. Escarpa, *Environ. Sci. Nano*, 2018, **5**, 2993–3003.

6 K. Emil, E. Berta, B. G. Mara, A. Pavimol, S. Tang, M. U. Rodolfo, F. Zhang, Z. Jing, L. Zhang and J. Wang, *ACS Nano*, 2018, **12**, 8397–8405.

7 M. Ibele, T. E. Mallouk and A. Sen, *Angew. Chem., Int. Ed.*, 2009, **48**, 3308–3312.

8 K. Villa, F. Novotny, J. Zelenka, M. P. Browne, T. Ruml and M. Pumera, *ACS Nano*, 2019, **13**, 8135–8145.

9 K. Yuan, V. Asunción-Nadal, B. Sánchez and A. Escarpa, *Chem. Mater.*, 2020, **32**, 1983–1992.

10 L. Kong, C. C. Mayorga-Martinez, J. Guan and M. Pumera, *Small*, 2020, **16**, e1903179.

11 R. Dong, Y. Cai, Y. Yang, W. Gao and B. Ren, *Acc. Chem. Res.*, 2018, **51**, 1940–1947.

12 Y. Wu, R. Dong, Q. Zhang and B. Ren, *Nanomicro Lett.*, 2017, **9**, 30.

13 Q. Zhang, R. Dong, Y. Wu, W. Gao, Z. He and B. Ren, *ACS Appl. Mater. Interfaces*, 2017, **9**, 4674–4683.

14 J. Wang, R. Dong, Q. Yang, H. Wu, Z. Bi, Q. Liang, Q. Wang, C. Wang, Y. Mei and Y. Cai, *Nanoscale*, 2019, **11**, 16592–16598.

15 A. M. Brooks, M. Tasinkevych, S. Sabrina, D. Velegol, A. Sen and K. J. M. Bishop, *Nat. Commun.*, 2019, **10**, 495.

16 L. Adams, D. Lee, Y. Mei, D. A. Weitz and A. A. Solovev, *Adv. Mater. Interfaces*, 2020, **7**, 1901583.

17 X. Lou, N. Yu, K. Chen, X. Zhou, R. Podgornik and M. Yang, *Chin. Phys.*, 2021, **30**, 119–124.

18 Q. Wang, C. Wang, R. Dong, Q. Pang and Y.-p. Cai, *Inorg. Chem. Commun.*, 2018, **91**, 1–4.

19 T. Maric, M. Nasir, R. D. Webster and M. Pumera, *Adv. Funct. Mater.*, 2020, **30**, 1908614.

20 A. M. Pourrahimi, K. Villa, Y. Ying, Z. Sofer and M. Pumera, *ACS Appl. Mater. Interfaces*, 2018, **10**, 42688–42697.

21 M. B. Tahir, G. Nabi, N. R. Khalid and M. Rafique, *Ceram. Int.*, 2017, S0272884217329322.

22 D. Zhou, Y. C. Li, P. Xu, N. S. Mccool, L. Li, W. Wang and T. E. Mallouk, *Nanoscale*, 2017, **9**, 75–78.

23 R. Dong, Y. Hu, Y. Wu, W. Gao, B. Ren, Q. Wang and Y. Cai, *J. Am. Chem. Soc.*, 2017, **139**, 1722–1725.

24 Y. Xing, X. Wang, S. Hao, X. Zhang and X. Xu, *Chin. Chem. Lett.*, 2020, **32**, 13–20.

25 X. Fei, H. Tan, B. Cheng, B. Zhu and L. Zhang, *Acta Phys. Chim. Sin.*, 2020, 2010027.

26 B. Yuan, J. Wei, T. Hu, H. Yao, Z. Jiang, Z. Fang and Z. Chu, *Chin. J. Catal.*, 2015, **36**, 1009–1016.

27 C. Han, J. Li, Z. Ma, H. Xie, G. I. N. Waterhouse, L. Ye and T. Zhang, *Sci. China Mater.*, 2018, **61**, 1159–1166.

28 Z. Li, Y. Ma, X. Hu, E. Liu and J. Fan, *Chin. J. Catal.*, 2019, **40**, 434–445.

29 K. Villa, C. L. Manzanares Palenzuela, Z. Sofer, S. Matejkova and M. Pumera, *ACS Nano*, 2018, **12**, 12482–12491.

30 Z. Ye, Y. Sun, H. Zhang, B. Song and B. Dong, *Nanoscale*, 2017, **9**, 18516–18522.

31 S. Liu, J. Sun and Z. Huang, *J. Hazard. Mater.*, 2010, **173**, 377–383.

32 M. S. Solís and A. F. Arias, *Carbon*, 2009, **47**, 2281–2289.

33 M. Yu, H. Liang, R. Zhan, L. Xu and J. Niu, *Chin. Chem. Lett.*, 2020, **32**, 2155–2158.

34 A. Dementjev, A. D. Graaf, d. Van K. Maslakov, A. Naumkin and A. Serov, *Diam. Relat. Mater.*, 2000, **9**, 1904–1907.

35 L. Yang, Z. Huang, G. Li, W. Zhang, R. Cao, C. Wang, J. Xiao and D. Xue, *Angew. Chem., Int. Ed.*, 2018, **130**, 1986–1990.

36 Y. Yang, C. Lu, J. Ren, X. Li and X. Zhao, *Ceram. Int.*, 2020, **46**, 5725–5732.

37 Y. Zheng, L. Lin, X. Ye, F. Guo and X. Wang, *Angew. Chem., Int. Ed.*, 2014, **53**, 11926–11930.

38 S. K. Ponnaiah, P. Prakash and S. Muthupandian, *Ultrason. Sonochem.*, 2019, **58**, 104629.

39 Y. Ren, Y. Li, X. Wu, J. Wang and G. Zhang, *Chin. J. Catal.*, 2021, **42**, 69–77.

40 S. Asadzadeh-Khaneghah, A. Habibi-Yangjeh and M. Abedi, *Separ. Purif. Technol.*, 2018, **199**, 64–77.

41 H. Liu, Z. Xu, Z. Zhang and D. Ao, *Appl. Catal., B*, 2016, **192**, 234–241.

42 Y. Ren, D. Zeng and W. J. Ong, *Chin. J. Catal.*, 2019, **40**, 289–319.

43 T. Xiong, W. Cen, Y. Zhang and F. Dong, *ACS Catal.*, 2016, **6**, 2462–2472.

44 R. Maria-Hormigos, B. Jurado-Sánchez and A. Escarpa, *Angew. Chem., Int. Ed.*, 2019, **131**, 3160–3164.

45 S. Asadzadeh-Khaneghah and A. Habibi-Yangjeh, *J. Clean. Prod.*, 2020, **276**, 124319.

46 X. Liu, R. Ma, L. Zhuang, B. Hu, J. Chen, X. Liu and X. Wang, *Crit. Rev. Environ. Sci. Technol.*, 2021, **51**, 751–790.

47 H. Eskandarloo, A. Kierulf and A. Abbaspourrad, *Nanoscale*, 2017, **9**, 13850–13863.

48 B. J. Sánchez and J. Wang, *Environ. Sci.: Nano*, 2018, **5**, 1530–1544.